

Charge Carrier Lifetime Determination in Graded Absorber Solar Cells Using Time-Resolved Photoluminescence Simulations and Measurements

Alexandra M. Bothwell,\* Carey L. Reich, Adam H. Danielson, Arthur Onno, Zachary C. Holman, Walajabad S. Sampath, and Darius Kuciauskas\*

Thin-film photovoltaic device efficiencies are limited by carrier recombination, thus understanding recombination mechanisms is critical for performance improvements. Bulk minority carrier lifetime  $(\tau_{bulk})$  is a critical parameter for solar cells but is difficult to determine in P-N junction devices, especially for high doping. As doping ≥10<sup>16</sup> cm<sup>3</sup> is required for efficient drift-charge-carriercollection devices, a method for  $\tau_{\text{bulk}}$  determination in doped P–N junction devices is necessary. This work utilizes time-resolved photoluminescence (TRPL) simulations to quantify bulk and interface recombination properties in highly doped, graded absorber CdSeTe structures. The two methods developed here for  $\tau_{bulk}$  determination include utilization of an instantaneous lifetime representation to guide TRPL fitting and direct comparison between measured and simulated decays. Simulations verified that both methods are valid for state-of-the-art device architectures which include graded bandgap absorbers, graded doping, and graded lifetimes. Shifts in the dominant recombination mechanism are identified for sufficiently long  $\tau_{bulk}$ , where front and back interface quality plays a more prominent role. Evaluation of surface recombination velocities and conduction band offset illustrate electro-optical advantages of a positive conduction band offset and highlight the necessity of improved interfaces as bulk quality in photovoltaic devices improves.

A. M. Bothwell, D. Kuciauskas
National Renewable Energy Laboratory
Golden, CO 80401, USA
E-mail: a.bothwell3@gmail.com; Darius.Kuciauskas@nrel.gov
C. L. Reich, A. H. Danielson, W. S. Sampath
Department of Mechanical Engineering
Colorado State University
Fort Collins, CO 80523, USA

A. Onno, Z. C. Holman School of Electrical, Computer and Energy Engineering Arizona State University Tempe, AZ 85287, USA

The ORCID identification number(s) for the author(s) of this article can be found under https://doi.org/10.1002/solr.202201029.

© 2023 The Authors. Solar RRL published by Wiley-VCH GmbH. This is an open access article under the terms of the Creative Commons Attribution-NonCommercial-NoDerivs License, which permits use and distribution in any medium, provided the original work is properly cited, the use is noncommercial and no modifications or adaptations are made.

DOI: 10.1002/solr.202201029

## 1. Introduction

Cadmium telluride (CdTe)-based solar cell technology has demonstrated high efficiency, manufacturing growth, and precipitous cost reduction in the last decade. [1,2] Efficiency records of 22.1% for solar cells and 19.1% for modules originated from short-circuit current density (JSC) and fill factor (FF) increases to 99% and 88% of their Shockley-Queisser (SQ) limits, respectively.<sup>[2-4]</sup> Only 79% of the SQ open-circuit voltage (VOC) has been realized, which is attributed to charge carrier recombination.<sup>[2-4]</sup> Therefore, recombination source identification and mitigation is a primary research focus. This is also the case for all solar cell technologies because defect density reduction in large-area semiconductor structures fabricated by fast growth processes is difficult.

Time-resolved photoluminescence (TRPL) measurements are typically utilized to characterize recombination in direct bandgap material structures and semiconductor solar cells such as CdTe. Electro-

optical (EO) properties such as bulk Shockley–Read–Hall (SRH) recombination lifetime ( $\tau_{bulk}$ ), front and back surface recombination velocities ( $S_{front}$  and  $S_{back}$ ), and electron and hole mobilities ( $\mu_e$  and  $\mu_h$ ), all of which significantly impact solar cell efficiencies, [5–8] can be determined from TRPL decay analysis. [9–13]

Historically, analysis of biexponential TRPL decays included exponential fitting to the initial part of the decay (often called " $\tau_1$ ") and the tail part of the decay (" $\tau_2$ " or " $\tau_{tail}$ "). These two regions and their corresponding lifetimes have been used to describe the physical processes of charge separation and minority carrier recombination, respectively. [11] The use of  $\tau_{tail}$  as an approximation for  $\tau_{bulk}$  is valid for structures with no P–N junction or space-charge field, such as double heterostructures, [14–16] or when applied voltage partially screens the field. [17] However, in structures with a space charge field and/or increased absorber doping, determination of  $\tau_{bulk}$  becomes less straightforward:  $\tau_{tail}$  may over or underestimate  $\tau_{bulk}$  due to interface recombination, radiative recombination, charge storage, and somewhat subjective fit regions. [17–19] For example, Moseley et al. demonstrated

www.solar-rrl.com

Solar

that  $\tau_{tail}$  correctly approximates  $\tau_{bulk}$  for SnO<sub>2</sub>/CdSeTe/CdTe devices (representative of First Solar's device structures) when absorber acceptor concentration  $N_A = 1 \ 10^{14} \ cm^3$  and  $S_{front}$ ,  $S_{back} < 100 \ cm \ s^1.^{[18]}$  However, charge storage, drift, and radiative recombination effects constrain such determination when  $N_A = 1 \ 10^{16} \ cm^3.^{[18]}$ 

The decline of accurate  $\tau_{bulk}$  determination for higher doping levels is a significant limitation because doping  $N_A \geq 10^{14}~cm^3$  is needed in photovoltaic devices where minority charge carrier collection is aided by the junction field. Arsenic-doped CdTe devices have reached doping levels of  $10^{15}$ – $10^{16}~cm^3$ , [20–22] Cu(In,Ga)Se<sub>2</sub> (CIGS) solar cell doping levels are typically  $10^{15}$ – $10^{16}~cm^3$  due to intrinsic defects,[23–27] and doping in perovskite solar cells can exceed  $10^{16}~cm^3$ . [28] Therefore, bulk recombination lifetime determination in doped absorbers is relevant for multiple PV technologies.

We present a simulation-based approach to understand bulk properties and quantify t<sub>bulk</sub> in P-N junction devices, with focus on group V-doped graded cadmium selenium telluride (CdSeTe/CdTe) with  $N_A = 1 \cdot 10^{15} \text{ cm}^3$ . Recently, such devices demonstrated high external radiative efficiency (ERE > 10<sup>3</sup>).<sup>[29]</sup> CdSeTe/CdTe solar cells have complex absorber composition, with intentionally graded (depth-dependent) absorber bandgap  $(E_{\sigma})$ , lifetime, and radiative efficiency. Thus, we consider the most complex state-of-the-art thin film solar cells. We demonstrate the utility of an instantaneous lifetime representation to provide consistent TRPL fit regions and a route to τ<sub>bulk</sub> determination. A direct-comparison approach between TRPL measurement and simulation is also implemented for  $\tau_{bulk}$  determination. We demonstrate that graded  $N_A = 1 \cdot 10^{14} - 1 \cdot 10^{15} \text{ cm}^3$  and graded  $\tau_{\text{bulk}}$  have perceptible effects on TRPL decays but neither inhibits the  $\tau_{\text{bulk}}$  analysis methodology developed here. Effects of interfaces are also analyzed, and variation of Sfront and Sback allows for the determination of front or back interface recombination contributions. Finally, the impacts of various EO parameters are illustrated more generally to guide interpretation of TRPL data.

# 2. Results and Discussion

Carrier dynamics encompass radiative and nonradiative, or Shockley-Read-Hall (SRH), recombination where SRH recombination can be described by bulk, front, and back interface recombination rates

$$\frac{1}{\tau_{TRPL}} \% \frac{1}{\tau_{SRH}} \flat \frac{1}{\tau_{rad}} \% \frac{1}{\tau_{bulk}} \flat \frac{1}{\tau_{front}} \flat \frac{1}{\tau_{back}} \flat \frac{1}{\tau_{rad}}$$
(1)

 $\tau_{front}$  corresponds to the minority carrier lifetime associated with recombination at the front (MgZnO/CdSeTe) interface,  $\tau_{back}$  to the minority carrier lifetime associated with recombination at the back (CdTe/Te) interface, and  $\tau_{rad}$  is radiative lifetime. Auger recombination is not considered in this work because it is an insignificant recombination mechanism in the direct bandgap CdSeTe/CdTe material. We vary  $\tau_{bulk}, \tau_{front},$  and  $\tau_{back}$  to identify recombination limiting mechanisms and compare these simulated results with experimental data.

### 2.1. Bulk Lifetime Analysis

To investigate bulk recombination,  $\tau_{bulk}$  = 10, 50, 100, 200, 400, 600, and 1000 ns were used as simulation inputs with  $N_A$  = 1  $10^{15}$  cm<sup>3</sup> and all other input parameters listed in Table 1. Interface recombination velocities ( $S_{front}$  = 100 cm s<sup>1</sup>,  $S_{back}$  = 1 10 cm & ) icorrespond to values for passivated CdSeTe/CdTe absorbers. Figure 1a compares simulated TRPL decays for  $\tau_{bulk}$  = 10, 100, and 1000 ns at excitation fluences 1  $10^{11}$  and 1  $10^{12}$  photons cm<sup>2</sup> pulse<sup>1</sup>. The normalized PL intensity range,  $10^4$ –1, is comparable with the experimentally accessible range in low injection measurements. Figure 1b provides the corresponding instantaneous lifetime,  $\tau_i$ , profiles, where  $\tau_i$  is based on the time-derivative of the PL intensity,  $I_{PL}$ 

$$\tau_i \frac{1}{4} \frac{P}{dt} \frac{1}{\underbrace{\delta tP}_{PL}} \frac{1}{dt}$$

Instantaneous lifetimes in Figure 1b are analyzed for the PL intensity range in Figure 1a, and therefore do not extend to 2000 ns in all cases. The logarithmic time axis is used to emphasize key aspects of the instantaneous lifetime data. For example, a constant  $\tau_i$  time range, which originates from unchanging carrier concentration, is visible. In particular, for the case of high bulk recombination ( $\tau_{bulk}$  = 10 ns) the constant  $\tau_i$  (t 2–30 ns) is approximately equal to  $\tau_{bulk}$ . This is in good agreement with the widely used TRPL tail-fit approach. For  $\tau_{bulk}$  = 100 ns, the constant  $\tau_i$  region extends to later times, and  $\tau_i$  is slightly less than  $\tau_{bulk}$  in this range. Instantaneous lifetimes exceed bulk lifetimes at t > 200 ns, which has been attributed to charge

Table 1. Simulation parameter inputs for a typical device.

	Parameter	Value	
Transparent conducting	Thickness	500 nm	
oxide (TCO)	Eg	3.6 eV	
	N <sub>D</sub> <sup>b</sup>	1 10 <sup>18</sup> cm <sup>3</sup>	
Buffer (MgZnO)	Thickness	100 nm	
	$E_g$	3.5 eV	
	$N_D^{\flat}$	1 10 <sup>14</sup> cm <sup>3</sup> 3.0	
Absorber (graded CdSeTe)	Thickness	μm	0.30
	Max Se composition [C <sub>0</sub> ]	1 10 <sup>14</sup> –1 10 <sup>15</sup> cm <sup>3</sup> 1	
	Carrier concentration, $[N_A]$	10 <sup>5</sup> cm <sup>1</sup> eV <sup>0.5</sup> 320 cm <sup>2</sup>	
	Absorption coefficient, $\left[\alpha_{0}\right]$	$V^1s^1$	$40 \text{ cm}^2 \text{ V}^1 \text{ s}^1$
	Electron mobility, $[\mu_{\text{e}}]$	2 10 <sup>10</sup> cm <sup>3</sup> s <sup>1</sup> þ0.2	
	Hole mobility, $[\mu_h]$	eV	100 cm
	Rad. recomb. coeff., [B <sub>rad</sub> ]	s <sup>1</sup>	
Front interface	Conduction band offset	1 10 <sup>4</sup> cm s <sup>1</sup> 0.0	
	$S_{front}$	V	640
Back interface	$S_{back}$	nm	60
	Back hole barrier	μm	
Characterization conditions	Laser wavelength	1.1 MHz	
	Laser beam diameter		
	Laser rep. rate		

Solar

www.advancedsciencenews.com www.solar-rrl.com

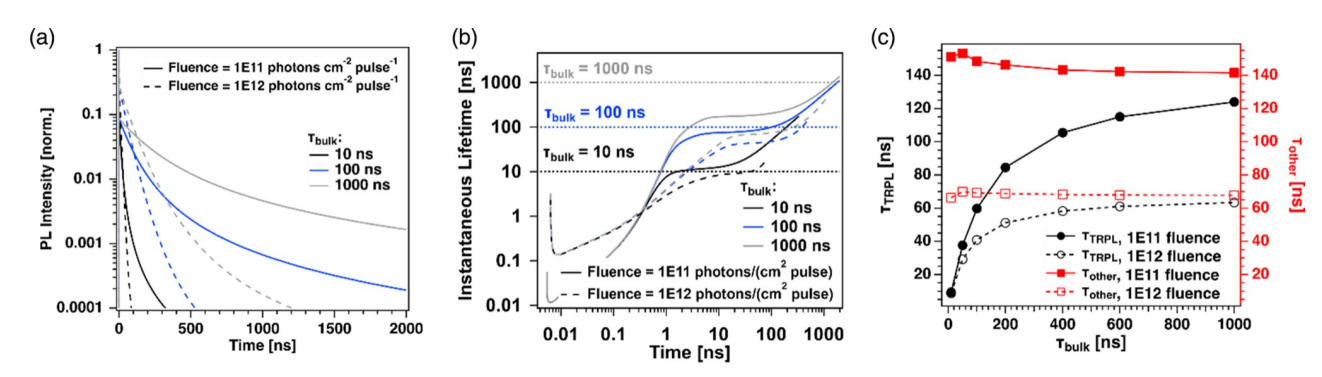


Figure 1. a) Simulated TRPL decays show slower decay with increasing bulk lifetime. Parameters used in simulation are summarized in Table 1, with  $N_A$  = 1  $10^{15}$  cm<sup>3</sup>. b) Instantaneous lifetime profiles show a constant instantaneous lifetime region which increases in value with greater bulk lifetime. Dotted lines correspond to  $\tau_{bulk}$  simulation input values. c) "Other" lifetime, which describes the lifetime differential between  $\tau_{bulk}$  and  $\tau_{TRPL}$  (fit in the constant  $\tau_{i}$  region), is approximately constant as a function of bulk lifetime.

storage. [18,19] For the longest bulk lifetimes ( $\tau_{bulk}$  = 1000 ns, as reported in passivated structures [31-33]), instantaneous lifetime profiles have similar constant regions, but  $\tau_i$  does not reach  $\tau_{bulk}$  value until very late times. This emphasizes that the typical determination of  $\tau_{bulk}$  by a fit to the tail of a TRPL decay can have a high degree of uncertainty, especially for devices with well-passivated interfaces.

As an alternative to TRPL tail fits, the flat  $\tau_i$  region can be utilized for  $\tau_{bulk}$  determination. A single exponential fit to the TRPL decay in the time range where  $\tau_i$  is constant yields  $\tau_{TRPL}$ , which is shown as a function of  $\tau_{bulk}$  on the left axis of Figure 1c. The asymptotic relationship indicates that  $\tau_{TRPL}$  underestimates  $\tau_{bulk}$  at long bulk lifetimes which is discussed further in Section 2.3. A re-representation of Equation (1) designates an "other lifetime,"  $\tau_{other}$ , which is comprised of  $\tau_{front}$ ,  $\tau_{back}$ , and  $\tau_{rad}$ 

$$\frac{1}{\tau_{TRPL}} \frac{1}{\sqrt{\tau_{bulk}}} \frac{1}{\tau_{front}} \frac{1}{\tau_{back}} \frac{1}{\tau_{rad}} \frac{1}{\sqrt{\tau_{bulk}}} \frac{1}{\tau_{other}}$$
(3)

The difference between  $\tau_{bulk}^{1}$  and  $\tau_{TRPL}^{1}$  enables calculation of  $\tau_{other}$  which, as shown on the right axis of Figure 1c, is approximately constant as a function of  $\tau_{bulk}$ . Given the dependence of  $\tau_{TRPL}$  on fluence,  $\tau_{other}$  is also dependent on fluence such that  $\tau_{other}^{143}$  ns for 1 10 11 photons cm<sup>2</sup> pulse 1 and 68 ns for 1  $10^{12}$  photons cm<sup>2</sup> pulse 1.

To determine  $\tau_{bulk}$  from a measured TRPL decay, this process can be reversed: rate  $\tau_{other}^{-1}$ , determined from the above-outlined simulation with values specific to the device structure and measurement conditions, is added to  $\tau_{TRPL}^{-1}$  to arrive at  $\tau_{bulk}$  according to Equation (3).

This approach has a few limitations. First, devices should have  $\tau_{bulk} > 100\,\mathrm{ns}$  because  $\tau_{other}$  is not constant at lower values. Second, it is also limited to TRPL measured at somewhat low fluence, <1  $10^{13}$  photons cm² pulse¹. At higher fluences, presented in the supplementary section, the flat  $\tau_i$  region disappears because the photogenerated carrier concentration is high enough that the carrier concentration profiles change across all time intervals. Finally, this approach requires EO parameter and device composition knowledge. For example, if the back interface is changed, the simulation process must be repeated with a new

 $S_{\rm back}$  value. The effects of altered parameters on instantaneous lifetime are provided in the Supporting Information.

A second method for  $\tau_{bulk}$  determination is through comparison between simulated and measured TRPL. Figure 2a shows TRPL data of As-doped structures (described in the Experimental Section) with a standard Te/C/Ni back contact (gray) and a passivating Al<sub>2</sub>O<sub>3</sub>/a-Si/ITO/Ag back contact (blue). Because the difference in these samples is the back contact structure, it can be reasonably assumed that the different TRPL tail lifetimes (102 ns for standard back contact and 166 ns for passivated back contact) can be attributed to variation in S<sub>back</sub>. Thus, simulations were executed with  $\tau_{bulk}$  varied and equal between samples, and S<sub>back</sub> varied and unequal between samples.

Figure 2a show good agreement between measured and simulated decays for  $\tau_{bulk,max}$  = 450 ns (where  $\tau_{bulk,max}$  corresponds to the maximum bulk lifetime in the graded absorber as shown in Figure 8b) and  $S_{back}$  = 5  $10^3$  and 800 cm s $^1$  for the standard and passivated back contacts, respectively. The bulk lifetime is longer than the tail fit results which emphasizes the uncertainty in TRPL fitting. This is expected based on Figure 1b,c results discussed above: for long  $\tau_{bulk}$  with fluence = 1  $10^{12}$  photons cm $^2$  pulse $^1$ , a fit to TRPL decay data at t > 200 ns will underestimate actual  $\tau_{bulk}$ .

Figure 2b shows the instantaneous lifetime profiles from the simulated decays. This highlights how changes in  $S_{back}$  materialize in the TRPL decay: the most prominent difference is exhibited in the flat  $\tau_i$  region. This is discussed in greater detail in Section 2.3.

## 2.2. Effects of Grading: Bulk Lifetime and Absorber Doping

Alloyed CdSeTe and group V doping are grading sources in CdTe device structures. This grading is used in all high-efficiency CdTe solar cells (as well as CIGS solar cells), and it is therefore critical to understand its impact. Multiple properties are depth-dependent (graded), and we consider three important categories. Graded bandgap, Eg, is included in all simulations and was implemented in Section 2.1. Here, we additionally consider effects due to grading of minority carrier lifetime (graded

www.advancedsciencenews.com www.solar-rrl.com



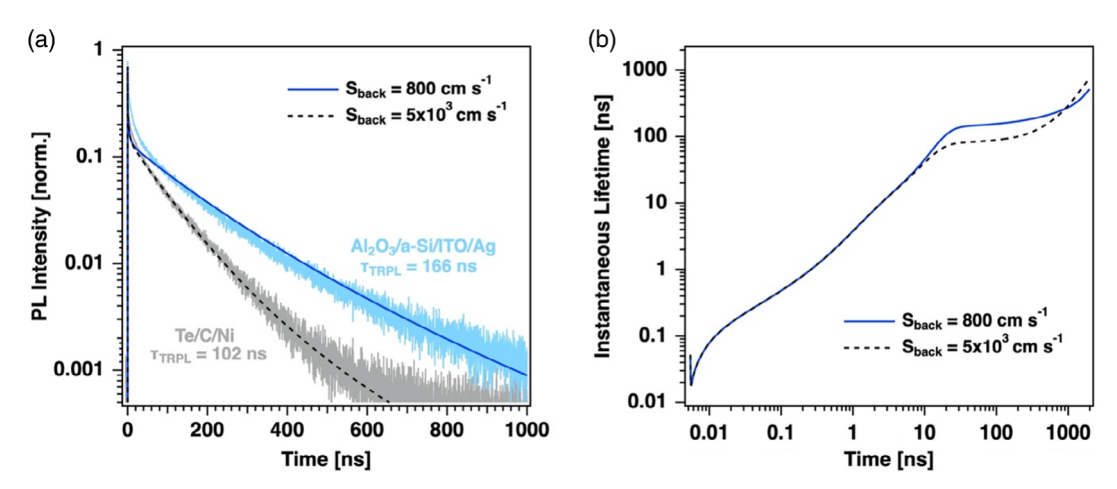


Figure 2. a) Measured TRPL decays of As-doped graded CdSeTe/CdTe structures with standard Te/C/Ni back contact (gray) and a passivating Al<sub>2</sub>O<sub>3</sub>/a-Si/ITO/Ag back contact (blue) compared to simulated decays suggest  $\tau_{\text{bulk},\text{max}}$  = 450 ns and  $S_{\text{back}}$  = 5 10<sup>3</sup> and 800 cm s<sup>1</sup> for the standard and passivated back contacts, respectively. b) Instantaneous lifetimes from the simulated decays highlight the greatest difference occurs in the flat  $\tau_i$  region.

 $\tau_{\text{bulk}}$ ) and absorber dopant density (graded  $N_A$ ). Because these properties are harder to measure, analysis is based on simulations.

The opposite  $\tau_{bulk}$  and  $N_A$  grading profiles (Figure 8b) originate from chemical composition and the method used to dope the absorber. Greater  $\tau_{bulk}$  near the front junction is due to the higher Se content. This was confirmed in experiments on nongraded absorbers with varying Se composition<sup>[33]</sup> and through cathodoluminescence (CL) measurements which consistently indicate higher radiative efficiency in regions with more Se.<sup>[34]</sup> In contrast to Se composition,  $N_A$  is higher at the back of the device due to the doping process which is enacted by As diffusion from the back of the structure. This approach mitigates effects of As accumulation near the front interface where As accumulation can lead to increased interface recombination.<sup>[22,35–37]</sup> The analytical models describing graded  $\tau_{bulk}$  and  $N_A$  profiles are approximations sufficient for this analysis.<sup>[21,22]</sup>

Figure 3a,c compares simulated TRPL decays and instantaneous lifetime profiles with and without  $\tau_{bulk}$  grading, given a fixed acceptor carrier concentration  $N_A = 1 \ 10^{15} \ cm^3$ . For short- and mid-range  $\tau_{bulk}$ , 10 and 100 ns respectively,  $\tau_{bulk}$  grading alters  $\tau_i$  in value but not time range of the flat  $\tau_i$  region. At longer  $\tau_{bulk}$ , 1000 ns, the grading has a much smaller effect on the TRPL decay: only small reductions in  $\tau_i$  in the flat  $\tau_i$  region are apparent. More specifically, there is a 20% relative decrease in  $\tau_i$  for  $\tau_{bulk} = 10 \ ns$ , a 16% relative decrease for  $\tau_{bulk} = 100 \ ns$ . Overall, the effect of  $\tau_{bulk}$  grading in this device structure is small, especially with long bulk lifetimes. This indicates that a 50%  $\tau_{bulk}$  grading profile should have only a small impact on TRPL interpretation.

Figure 3b,d compares TRPL decays and instantaneous lifetime profiles with and without  $N_A$  grading. Carrier concentration grading has a more notable effect than  $\tau_{bulk}$  grading: the initial and flat  $\tau_i$  time regions are both impacted. The early-time TRPL behavior, which is influenced in part by minority carrier drift, changes because the electric field is modified by varied

carrier concentration. The flat  $\tau_i$  region narrows and  $\tau_i$  decreases for lower carrier concentration. For the graded case  $N_A=1\ 10^{14}-1\ 10^{15}\ cm^3$ , the flat  $\tau$  range is closer to  $N_A=1\ 10^{15}\ cm^3$  than  $N_A=1\ 10^{14}\ cm^3$ , indicating the dominance of the more highly doped region. This implies that

with a transition from a traditional Cu-doped device ( $N_A = 1\ 10^{14}\ cm^3$ ) to a graded, As-doped device ( $N_A = 1\ 10^{14}-1\ 10^{15}\ cm^3$ ) one should expect a wider, higher value  $\tau$  region in addition to the slower TRPL decays observed with As doping. [22,32,35]

Grading results indicate that the utilization of the flat  $\tau_i$  region for TRPL fitting as described in the previous section is still applicable for absorbers with graded  $\tau_{bulk}$  and  $N_A$ . The flat  $\tau_i$  time range is slightly narrowed by  $N_A$  grading, and the value changes slightly due to both  $\tau_{bulk}$  and  $N_A$  grading, but it is still appropriate for  $\tau_{TRPL}$  extraction and  $\tau_{other}$  calculation.

### 2.3. Interface Recombination

### 2.3.1. Interface and Bulk Rate Relationships

Interface properties were investigated through varied front and back interface recombination velocity ( $S_{front}$  and  $S_{back}$ ) simulation inputs. This analysis underscores how recombination-limiting mechanisms depend on the interplay of  $\tau_{bulk}$  and  $S_{front}$  and  $S_{back}$ . We first consider cases when  $S_{front} = S_{back}$  and advance to variation of these values independently.

Figure 4a compares simulations for the representative ("typical") device structure discussed in the previous sections to the ideal interfaces case ( $S_{front} = S_{back} = 1 \text{ cm s}^1$ ; such ideal interfaces have been realized in single crystal CdTe<sup>[38]</sup>), with  $\tau_{bulk} = 10$ , 100, and 1000 ns. The difference between ideal versus typical interfaces becomes increasingly significant for longer bulk lifetimes as the dominant recombination mechanism shifts from bulk recombination to interface recombination. The  $\tau_i$  profiles in Figure 4b reveal that the recombination velocity modifications change TRPL decay in the flat  $\tau_i$  time range. In the case of short  $\tau_{bulk} = 10$  ns, the flat  $\tau_i$  values agree well with  $\tau_{bulk}$  because

from https://onlinelibrary.wiley.com/doi/10.1002/solr.202201029 by Colorado State University, Wiley Online Library on [08/06/2023]. See the Terms

of use; OA articles are governed by the applicable Creative Commons

www.advancedsciencenews.com www.solar-rrl.com

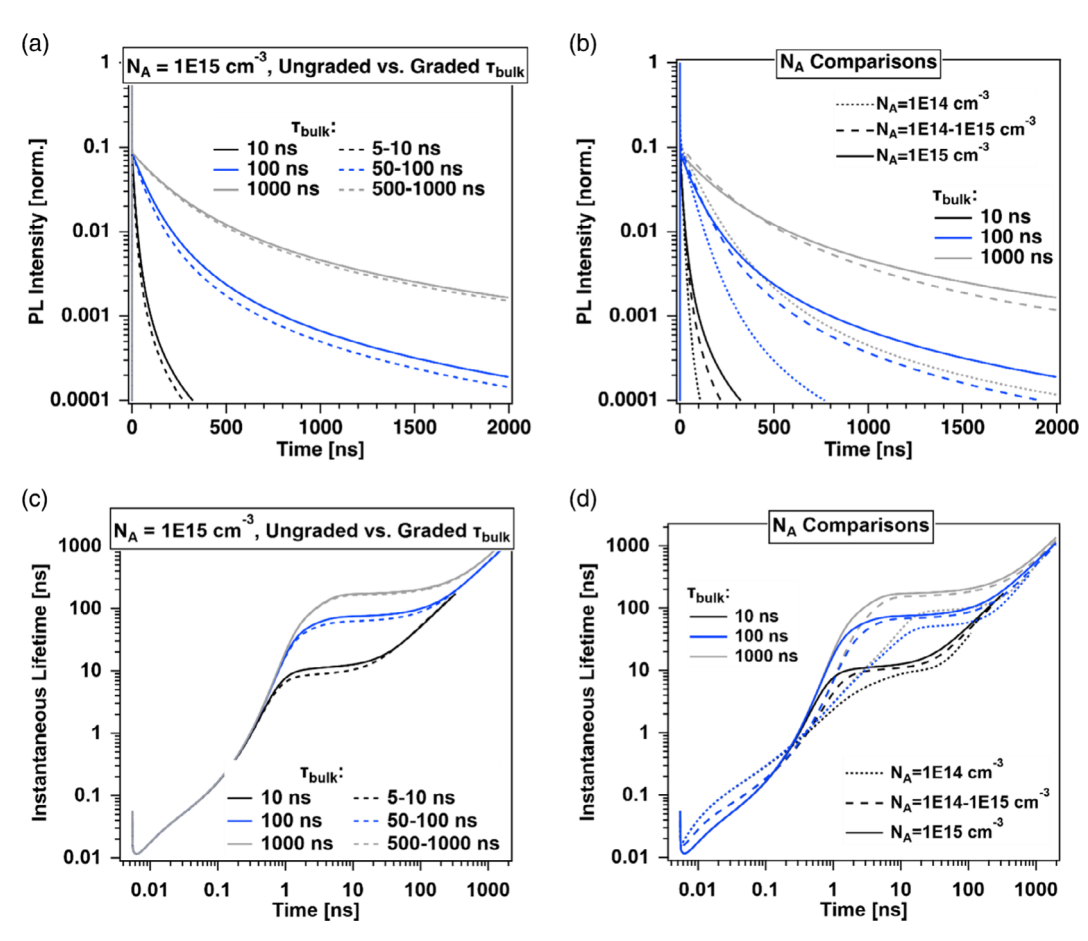


Figure 3. a) Simulated TRPL decays and c) instantaneous lifetime profiles show that bulk lifetime grading changes the value of the flat instantaneous lifetime region. Solid lines correspond to ungraded bulk lifetimes and dashed lifetimes correspond to graded bulk lifetimes. b) TRPL decays and d) instantaneous lifetime profiles show that N<sub>A</sub> grading changes the value and time range of the flat instantaneous lifetime region.

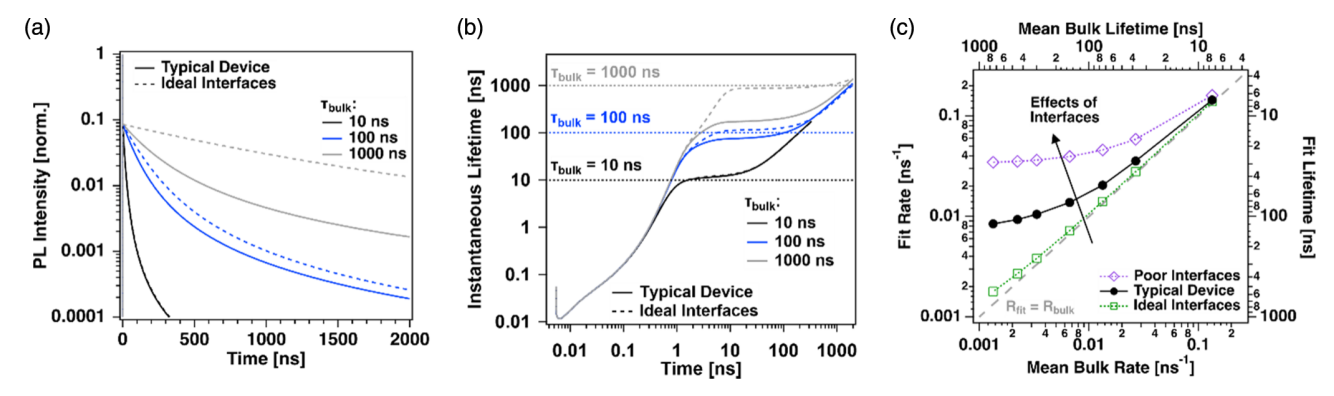


Figure 4. a) Simulated TRPL decays and b) instantaneous lifetime profiles for typical and ideal device interfaces with  $N_A = 1 \ 10^{15}$  cm. c) Mean rates and lifetimes extracted from the flat  $\tau_i$  region when graded bulk lifetime is varied. Interface effects are seen most prominently at short bulk rates (long bulk lifetimes). The following parameters are used in simulations: typical device:  $S_{front} = 100 \ cm \ s^1$ ,  $S_{back} = 1 \ 10^4 \ cm \ s^1$ . Ideal interfaces:  $S_{front} = 1 \ 10^4 \ cm \ s^1$ . Poor interfaces:  $S_{front} = 1 \ 10^4 \ cm \ s^1$ ,  $S_{back} = 1 \ 10^5 \ cm \ s^1$ .

it is the dominant recombination mechanism, and the effect of improved interfaces is negligible. As  $\tau_{bulk}$  increases, interface recombination plays a more dominant role; long  $\tau_{bulk}$  is only well matched by  $\tau_i$  if interface recombination velocities are low. In agreement with earlier sections, the flat  $\tau_i$  region is the critical

TRPL decay time range in which recombination-limiting mechanisms can be explored.

The impact of interface recombination is summarized in Figure 4c which shows TRPL fit rate  $R_{TRPL}$  (fit lifetime  $\tau_{TRPL}$ ) versus mean bulk rate  $R_{bulk}$  (graded lifetime  $\tau_{bulk}$ ) for simulated

www.solar-rrl.com

......

 $τ_{bulk,max}$  = 10–1000 ns in the case of ideal, typical, and poor interfaces. Lifetime  $τ_{TRPL}$  was determined by a single exponential TRPL fit in the flat  $τ_i$  time range and fit rate was calculated as  $τ_{TRPL}$ . The gray, dashed line represents the case without interface or radiative recombination ( $R_{TRPL}$  =  $R_{bulk}$ ,  $τ_{TRPL}$  =  $τ_{bulk}$ ). The  $R_{TRPL}$  versus  $R_{bulk}$  representation emphasizes the increasing impact of interfaces for longer  $τ_{bulk}$ : data essentially overlap at high bulk rates (short  $τ_{bulk}$ ) where bulk recombination is dominant and deviate from  $R_{TRPL}$  =  $R_{bulk}$  as  $τ_{bulk}$  improves. Increasingly poor interfaces are apparent at low bulk rates (long  $τ_{bulk}$ ) where interface recombination becomes the dominant recombination mechanism.

Figure 4c suggests that in a device with poor interfaces  $(S_{front}=1\ 10^4\ cm\ s^1,\ S_{back}=1\ 10^5\ cm\ s^1)$  bulk defect density reduction (improvements to  $\tau_{bulk}$ ) will not increase  $\tau_{TRPL}$  above 30 ns. In typical devices  $(S_{front}=100\ cm\ s\ ,S_{back}^1=1\ 10^4\ cm\ s^1),\ \tau_{TRPL}$  is limited to 100 ns. Therefore, as CdSeTe/CdTe bulk lifetimes continue to increase, there is an accompanied need for improved interfaces.

The impact of defects at front and back interfaces was investigated by analysis of TRPL sensitivity to independently varied  $S_{front}$  and  $S_{back}$  inputs. As excitation (and solar irradiation) occurs through the front interface and carriers are generated close to the

front contact,  $S_{front}$  impact on overall recombination might be expected to be higher. Alternatively, the electric field near the front interface (due to the P–N junction and absorber grading) might reduce the impact of  $S_{front}$ . Simulation results in Figure 5 enable an understanding of these contributions. Figure 5a,b present a case where  $S_{front}$  and  $S_{back}$  differ by  $10^4 \, \mathrm{cm \ s}^1$  and Figure 5c,d a case where  $S_{front}$  and  $S_{back}$  differ by  $100 \, \mathrm{cm \ s}^1$ . We consider short bulk lifetimes (Figure 5a,c) and long bulk lifetimes (Figure 5b,d). The ideal case,  $S_{front} = S_{back} = 1 \, \mathrm{cm \ s}^1$ , is given by the dashed lines for reference.

In all cases,  $S_{front}$  has a greater impact on lifetime than  $S_{back}$ , demonstrated by the higher  $\tau_i$  values for a minimized  $S_{front}$ . However, this impact is somewhat small, especially for the typical device structure that has been discussed (SRVs = 100 and 1  $10^4$  cm s<sup>1</sup>). These results hold regardless of bulk lifetime (compare Figure 5a,c–b,d). This suggests that regardless of absorber quality, reduction of  $S_{front}$  would be somewhat more favorable for improved carrier lifetime than  $S_{back}$  reduction. But data indicate that without at least one ideal interface, the differences are small.

Next, to quantify interface recombination rate,  $R_{\rm int}$  is calculated by (compare with Equation (1))

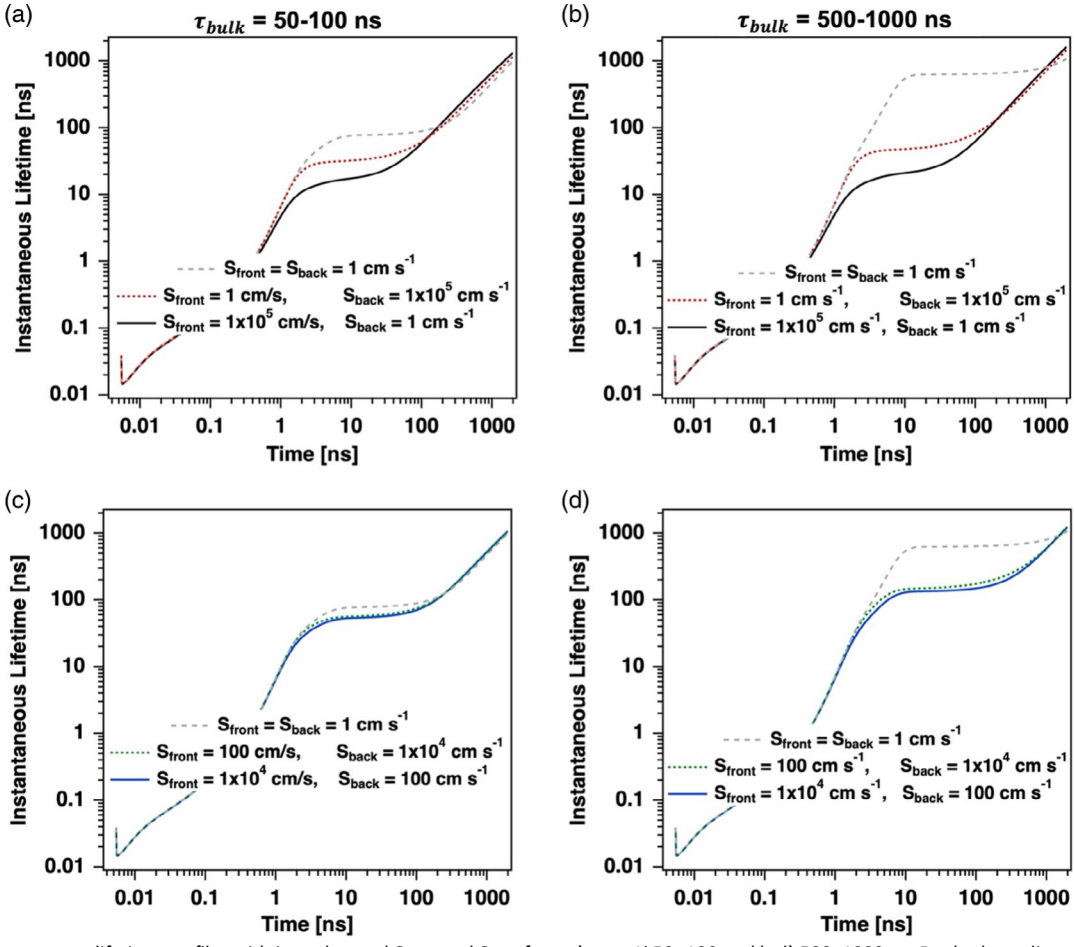


Figure 5. Instantaneous lifetime profiles with interchanged  $S_{front}$  and  $S_{back}$  for a,c)  $\tau_{bulk}$  ¼ 50–100 and b,d) 500–1000 ns. Dashed gray lines correspond to ideal interfaces  $S_{front}$  =  $S_{back}$  = 1 cm s<sup>1</sup>. Results indicate that  $S_{front}$  impacts TRPL more when the SRV differential is large.

www.advancedsciencenews.com

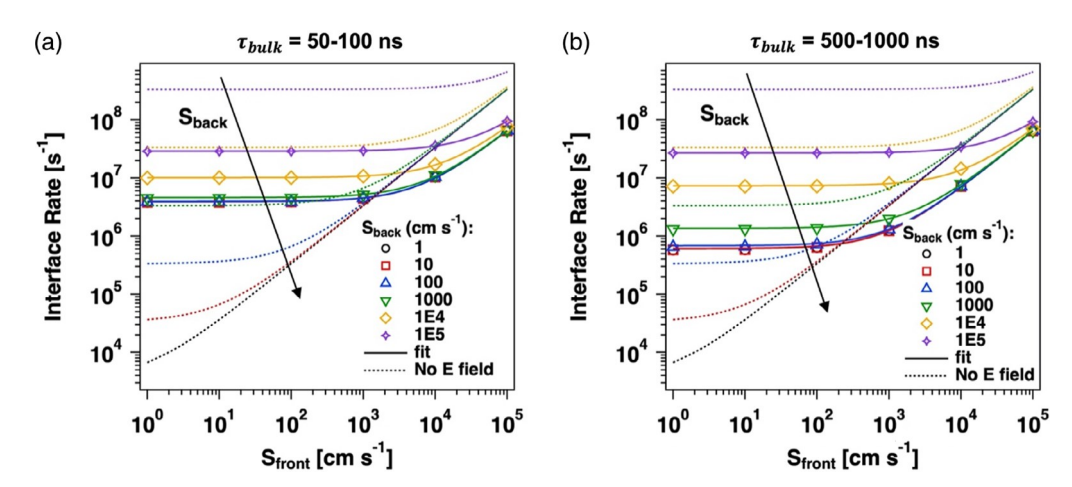


Figure 6. Interface rates as a function of  $S_{front}$  and  $S_{back}$  for graded  $\tau_{bulk}$  % 50–100 ns (a) and 500–1000 ns (b). Symbols are device simulation results and solid lines are corresponding fits to Equation (5) with independent fit parameters d for both interfaces. Dotted lines plot a field-free sample: Equation (5) where d is sample thickness.

$$R_{int} \% R_{TRPL} R_{bulk} R_{rad}$$
 (4)

where  $R_{rad} = N_A B_{rad}$  under a low injection condition like that investigated here.  $R_{int}$  versus  $S_{front}$  with discrete  $S_{back}$  values are given in Figure 6a,b for graded  $\tau_{bulk}$  = 50–100 and 500–1000 ns, respectively. Simulation results for devices, determined by Equation (4), are given by symbols. For samples without electric field<sup>[14]</sup>

$$R_{int} \% S_{front} = d \beta S_{back} = d$$
 (5)

where d is absorber thickness and recombination velocities derive from the interface defect density,  $N_{\rm int}$  (S  $v_{\rm th}\sigma N_{\rm int}$ , where  $v_{\rm th}$  is thermal velocity and  $\sigma$  is capture cross section). The dotted lines in Figure 6 show  $R_{\rm int}$  calculated from Equation (5) for sam-ples without an electric field; in most cases agreement with device simulations is poor.

The solid lines in Figure 6 apply the model of Equation (5) to the simulation results but adjust parameter d in the fit, independently for each interface. Employment of d as a floating parameter for fits creates a more realistic device description where carriers do not equally see each interface. Because fitted d values differ from the sample thickness, the fits indicate how the impact of front and/or back interface recombination differs in structures without an electric field versus devices. Comparison of solid lines (device) and dotted lines (absorber without electric field) shows that interface rates can be both higher and lower in devices, depending on  $\tau_{\text{bulk}}$ ,  $S_{\text{front}}$ , and  $S_{\text{back}}$ .

#### 2.3.2. Interface and Conduction Band Offset Relationships

The front-side conduction band offset (CBO) between the n-type buffer and p-type absorber (MgZnO and CdSeTe, respectively, in the structures presented here) significantly impacts carrier recombination and open-circuit voltage ( $V_{\rm OC}$ ), where  $V_{\rm OC}$  is maximized with CBO =  $p_{\rm OC}$  eV for MgZnO/CdSeTe device structures. [39,40] Here, we present the impact that CBO has on interface recombination.

Figure 7 compares interface recombination rates (determined by Equation (4)) for CBO =  $0.0 \, \text{eV}$  (Figure 7a,c) and  $\flat 0.2 \, \text{eV}$  (Figure 7b,d) with variation in  $S_{front}$  and  $S_{back}$ . For CBO =  $\flat 0.2 \, \text{eV}$ , the symmetric contours indicate that  $S_{front}$  and  $S_{back}$  contribute nearly equally to interface recombination. In contrast, for CBO =  $0.0 \, \text{eV}$  interface recombination is affected primarily by  $S_{front}$ . This indicates that with a spike-like,  $\flat 0.2 \, \text{eV}$  CBO, improvement to the front or back interface will equally reduce interface recombination but with a flat band,  $0.0 \, \text{eV}$  CBO, interface recombination is limited by  $S_{front}$ . These conclusions hold for short and long bulk lifetimes, exemplified by the unchanged contour symmetries in Figure 7a,c and b,d, with graded  $\tau_{bulk}$  = 50-100 and 500-1000 ns.

The different scales between Figure 7a,c and b,d highlight that CBO also impacts the range of achievable interface rates. This range is significantly lower and narrower for CBO =  $\flat 0.2$  eV than 0.0 eV. This indicates that CBO =  $\flat 0.2$  eV is superior for reduced interface recombination, in agreement with  $V_{\rm OC}$  and efficiency simulation and experimental results in the literature. [39,40]

Finally, the CBO has little impact on late decay times, which is discussed in greater detail in the supplementary material section. Therefore, to investigate CBO with TRPL, early decay times should be utilized. Results in the supplementary material show that variation of CBO has a smaller effect than properties analyzed in Section 2.1–2.3.1.

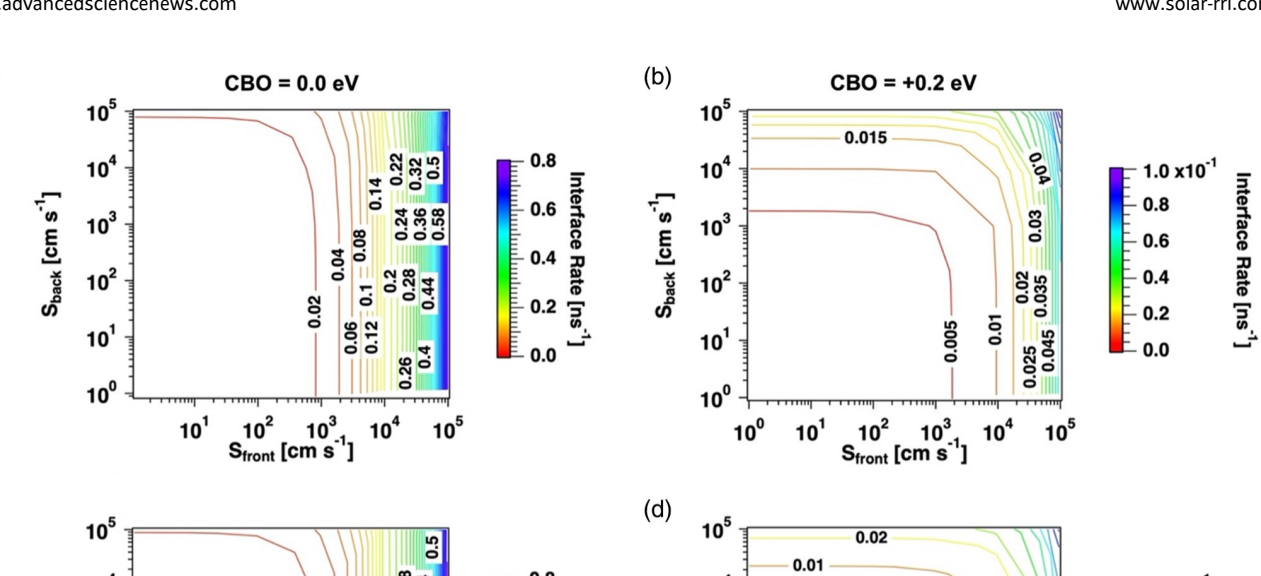
# 3. Conclusion

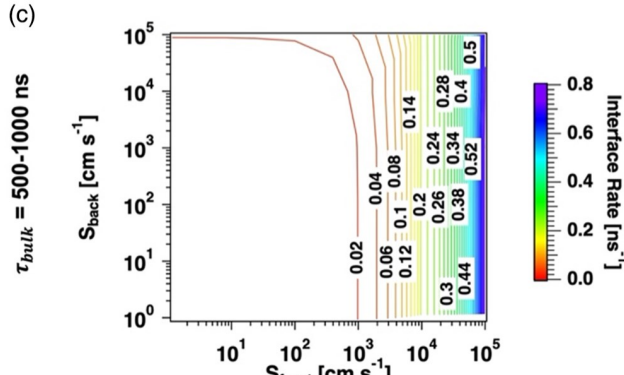
Minority carrier lifetime is a central parameter in PV materials. For Si PV, lifetimes are measured for wafers rather than devices. This is not viable for thin films where absorber properties change in device fabrication. Therefore, to determine carrier lifetimes in thin film solar cells, simulations of lifetime measurements such as TRPL are used. In this article, a simulation-based lifetime analysis methodology was developed which categorizes dominant carrier recombination mechanisms and enhances bulk

(a)

bulk = 50-100 ns

www.advancedsciencenews.com www.solar-rrl.com





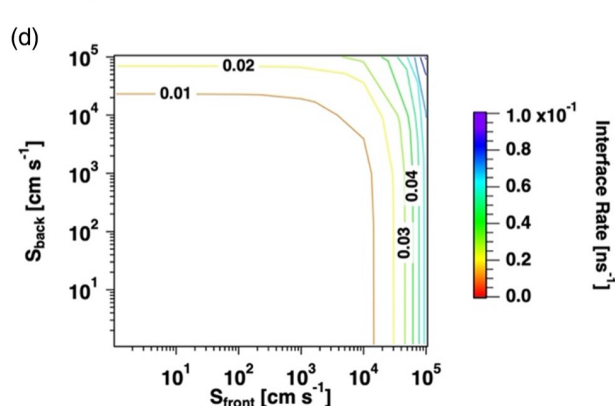


Figure 7. Interface rates as a function of  $S_{front}$  and  $S_{back}$  for  $\tau_{bulk}$  ½ 50–100 ns (a,b) and 500–1000 ns (c,d) for CBOs = 0 eV and  $\varphi$ 0.2 eV, respectively.

carrier lifetime determination for graded absorber CdSeTe solar cells doped at  $10^{15} \, \text{cm}^3$ .

Two TRPL simulation methods were developed to reduce the ambiguity of bulk lifetime determination in group V-doped CdSeTe devices with a P–N junction. First, the flat instantaneous lifetime region was utilized to establish a well-defined TRPL fit range compared to the often-indefinite tail fit region in traditional TRPL fitting processes. This flat  $\tau_i$  region was used to calculate  $\tau_{\rm bulk}.$  Second, comparisons between simulations and measured TRPL data provided more explicit bulk lifetime quantification as well as information about additional electro-optical properties.

Graded lifetimes and acceptor carrier concentrations—associated with long-lifetime graded CdSeTe absorbers and high, group V doping at the back of devices—impacted TRPL decay shapes but did not nullify the  $\tau_{bulk}$  determination methods described above.  $\tau_{bulk}$  grading had a non-negligible impact at short bulk lifetimes and less impact at longer bulk lifetimes. Carrier concentration grading demonstrated a change in early-time TRPL behavior due to the electric field modification by carrier concentration gradients, as well as at later times where  $\tau_i$  decreased for lower carrier concentration.

The flat  $\tau_i$  region also highlighted recombination-limiting mechanisms. The difference in  $\tau_i$  between ideal and typical interface cases increased significantly for longer  $\tau_{bulk}$ , dictated by the shift in dominant recombination mechanism from bulk to interface recombination. This highlights the necessity of improved

interfaces as CdSeTe bulk quality improves. Independent impacts of front and back interface recombination velocities revealed that  $S_{\rm front}$  has a somewhat greater impact on fit lifetime than  $S_{\rm back}$ , although this impact is fairly small, especially for the typical CdSeTe device which was primarily discussed. Comparison of flat-band, 0.0 eV and spike-like,  $\rm b0.2$  eV front-side CBOs demonstrated the advantages of a positive CBO. It reduces interface recombination, in agreement with  $\rm V_{\rm OC}$  and efficiency simulation and experimental results in the literature.  $\rm ^{[39,40]}$  These results can be utilized to direct research focus between bulk and interface defect density reduction for a more targeted approach to photovoltaic efficiency increases.

### 4. Experimental Section

COMSOL Simulation: TRPL decays were simulated using a COMSOL application, [41] in which the time-dependent electron and hole continuity equations and Poisson's equation are solved after pulsed laser excitation to generate recombination rate components. Carrier generation is from the front, or glass-side of a superstrate-configured device, and as described by Moseley et al., many additional parameters can be varied as simulation inputs. [18] The simulation application is publicly available. [41]

Simulation inputs were established based on the As-doped CdSeTe devices fabricated at Colorado State University which were measured for experimental comparison. The device structure is given in Figure 8a. Absorber composition grading, which is consistent throughout this work, is given by  $y(x) = C_0 erf(x/L)$  with exponential-like decreasing Se

are governed by the applicable Creative Commons

www.advancedsciencenews.com www.solar-rrl.com

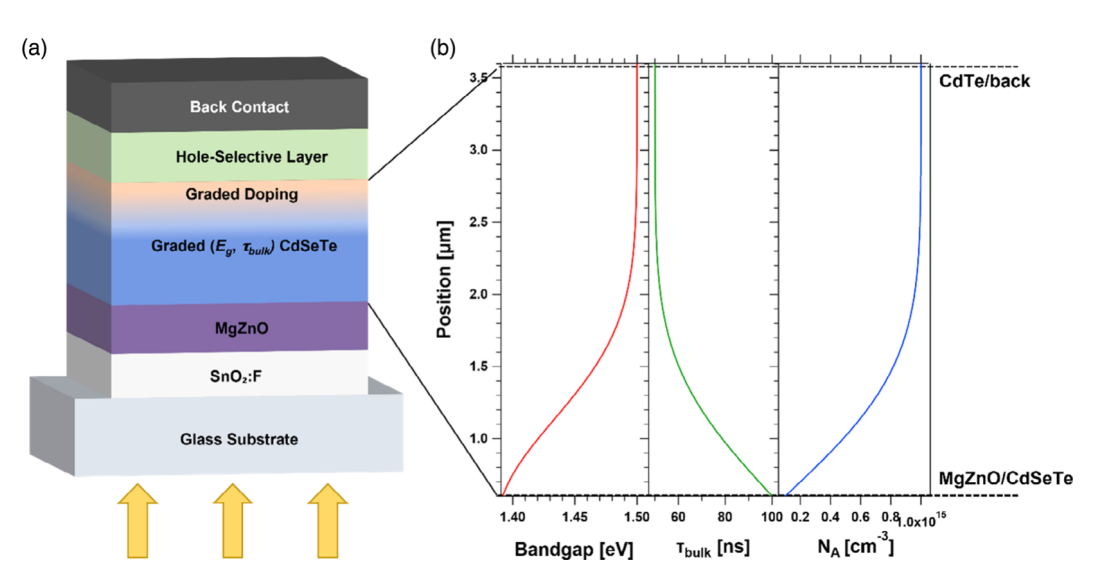


Figure 8. a) Graded CdSeTe/CdTe absorber structure (not to scale). b) Bandgap, bulk lifetime, and acceptor concentration grading in the absorber are assumed to derive from chemical composition and follow similar grading profiles.

composition from the front to back interface. y is the fraction of anion sites occupied by Se,  $C_0$  is maximum Se composition, x is absorber depth, and L is a length-scaling constant. Composition grading dictates the absorber bandgap,  $E_g(\gamma)=1.5(1y) \not p \ 1.7y0.8y(1y).^{[18]}$  Here,  $C_0=0.30$  and L = 1  $\mu m$  such that E varies from 1.39 eV at the front MgZnO/CdSeTe interface to 1.50 eV at the back interface as shown in Figure 8b.  $^{[34,42]}$  Figure 8a,b also highlights the additional graded parameters,  $\tau_{bulk}$  and  $N_A$ , investigated in this work. Additional input parameters are given in Table 1 with values held fixed unless otherwise specified.  $^{[6,12,22,39]}$ 

Structure Fabrication and Characterization: Structures were fabricated on a SnO<sub>2</sub>:F/100 nm MgZnO substrate. The first device architecture was 0.5 μm CdSeTe:As/2.6 μm CdTe/200 nm CdSeTe:As/Te/C/Ni, referred to as the standard back contact, and the second was 0.5  $\mu m$  CdSeTe/ 3.0 µm CdTe/200 nm CdSeTe:As/Al<sub>2</sub>O<sub>3</sub>/a-Si/ITO/Ag, referred to as the passivated back contact. Structures were not delineated into individual devices. The n-type MgZnO buffer layer was RF sputter-deposited on SnO2:F-coated glass (Pilkington Tec10), followed by close-space sublimation-deposited CdSeTe and CdTe and CdCl2 passivation treatment. Devices were As-doped through a cosublimation process under Cd overpressure using predoped CdSe<sub>0.4</sub>Te<sub>0.6</sub> material. Acceptor concentration in finished devices was  $N_A$  1  $10^{15}\,\text{cm}^3$  for both structures. measured by capacitance-voltage. Standard back contact devices were finished with 30 nm of evaporated Te and spray-coated carbon and nickel paints. Passivated devices were finished with a 2 nm magnetron sputtered Al<sub>2</sub>O<sub>3</sub> layer followed by an 8 nm p-type boron-doped hydrogenated amorphous silicon (a-Si:H(p)) layer deposited by plasma-enhanced chemical vapor deposition, and finally, a 70 nm ITO/200 nm Ag back electrode was deposited by reactive sputtering. Additional fabrication details can be found in the literature. [12,29]

TRPL was measured using excitation at 640 nm with fluence =  $1.0 \ 10^{12}$  photons cm² pulse¹, incident on the front MgZnO/CdSeTe side of the structure. Excitation wavelength was controlled by an optical parametric amplifier (OPA) and 0.3 ps pulses at a 1.1 MHz repetition rate were used. Time-correlated single photon counting was implemented for TRPL decay detection. [43]

# Supporting Information

Supporting Information is available from the Wiley Online Library or from the author.

# Acknowledgements

This work was authored in part by the National Renewable Energy Laboratory, operated by Alliance for Sustainable Energy, LLC, for the U.S. Department of Energy (DOE) under Contract No. DE-AC36-08GO28308. Funding provided by U.S. Department of Energy Office of Energy Efficiency and Renewable Energy Solar Energy Technologies Office. The views expressed in the article do not necessarily represent the views of the DOE or the U.S. Government. This article has been contributed to by US Government contractors and their work is in the public domain in the USA. The information, data, or work presented herein was funded in part by the U.S. Department of Energy, Office of Energy Efficiency and Renewable Energy, under award number DE-EE0008552.

### Conflict of Interest

The authors declare no conflict of interest.

# Data Availability Statement

The data that support the findings of this study are available from the corresponding author upon reasonable request.

## Keywords

carrier lifetime, doping, interfaces, solar cells, time-resolved photoluminescence

Received: November 15, 2022 Revised: January 13, 2023 Published online: February 28, 2023

S. Philipps, Photovoltaics Report, Fraunhofer Institute for Solar Energy Systems ISE Press and Public Relations, Freiburg, Germany 2022.

<sup>[2]</sup> M. A. Scarpulla, B. McCandless, A. B. Phillips, Y. Yan, M. J. Heben, C. Wolden, G. Xiong, W. K. Metzger, D. Mao, D. Krasikov, I. Sankin,

www.advancedsciencenews.com www.solar-rrl.com

- S. Grover, A. Munshi, W. Sampath, J. R. Sites, A. Bothwell, D. Albin, A. Romeo, M. Nardone, R. Klie, J. M. Walls, T. Fiducia, A. Abbas, Sol. Energy Mater. Sol. Cells, 2023, accepted.
- [3] M. Green, E. Dunlop, J. Hohl-Ebinger, M. Yoshita, N. Kopidakis, X. Hao, Prog. Photovoltaics: Res. Appl. 2021, 29, 3.
- [4] R. M. Geisthardt, M. Topič, J. R. Sites, IEEE J. Photovolt. 2015, 5, 1217.
- [5] G. K. Liyanage, A. B. Phillips, F. K. Alfadhili, R. J. Ellingson, M. J. Heben, ACS Appl. Energy Mater. 2019, 2, 5419.
- [6] R. Pandey, T. Shimpi, A. Munshi, J. R. Sites, IEEE J. Photovolt. 2020, 10, 1918.
- [7] J. N. Duenow, W. K. Metzger, J. Appl. Phys. 2019, 125, 053101.
- [8] A. Kanevce, M. O. Reese, T. Barnes, S. Jensen, W. Metzger, J. Appl. Phys. 2017, 121, 214506.
- [9] D. Kuciauskas, in Advanced Characterization of Thin Film Solar Cells (Eds: M. Al-Jassim, N. Haegel), IET Energy Engineering Series, Vol. 166, London, UK 2020.
- [10] M. Maiberg, C. Spindler, E. Jarzembowski, R. Scheer, Thin Solid Films 2015, 582, 379.
- [11] A. Kanevce, D. Levi, D. Kuciauskas, Prog. Photovolt. Res. Appl. 2014, 22. 1138.
- [12] A. Danielson, D. Kuciauskas, C. Reich, S. Li, A. Onno, W. Weigand, A. Kindvall, A. Munshi, Z. Holman, W. Sampath, 47th IEEE Photovoltaic Specialists Conf. (PVSC), IEEE, Piscataway, NJ 2020, pp. 1811–1812.
- [13] A. Kanevce, D. Kuciauskas, T. A. Gessert, D. H. Levi, D. S. Albin, 38th IEEE Photovoltaic Specialists Conf., IEEE, Piscataway, NJ 2012, pp. 000848–000853.
- [14] K. N. Zaunbrecher, D. Kuciauskas, C. H. Swartz, P. Dippo, M. Edirisooriya, O. S. Ogedengbe, S. Sohal, B. L. Hancock, E. G. LeBlanc, P. A. Jayathilaka, Appl. Phys. Lett. 2016, 109, 091904.
- [15] R. K. Ahrenkiel, Semicond. Semimetals 1993, 39.
- [16] E. Perl, D. Kuciauskas, J. Simon, D. Friedman, M. Steiner, J. Appl. Phys. 2017, 122, 233102.
- [17] P. M. Jundt, D. Kuciauskas, J. R. Sites, IEEE J. Photovolt. 2021, 12, 501.
- [18] J. Moseley, D. Krasikov, C. Lee, D. Kuciauskas, J. Appl. Phys. 2021, 130,
- [19] M. Maiberg, T. Hölscher, S. Zahedi-Azad, R. Scheer, J. Appl. Phys. 2015, 118, 105701.
- [20] W. K. Metzger, S. Grover, D. Lu, E. Colegrove, J. Moseley, C. Perkins, X. Li, R. Mallick, W. Zhang, R. Malik, Nat. Energy 2019, 4, 837.
- [21] E. Colegrove, B. Good, A. Abbas, H. Moutinho, S. Johnston, C.-S. Jiang, P. O'Keefe, J. M. Walls, D. S. Albin, M. O. Reese, Sol. Energy Mater. Sol. Cells 2022, 246, 111886.
- [22] A. Danielson, C. Reich, R. Pandey, A. Munshi, A. Onno, W. Weigand, D. Kuciauskas, S. Li, A. Bothwell, J. Guo, M. Murugeson, J. S. McCloy, Z. C. Holman, W. Sampath, Sol. Energy Mater. Sol. Cells 2023, 251, 112110
- [23] N. Mufti, T. Amrillah, A. Taufiq, M. Diantoro, H. Nur, Sol. Energy 2020, 207, 1146.

- [24] M. Asaduzzaman, M. Hasan, A. N. Bahar, SpringerPlus 2016, 5, 1.
- [25] S. Shirakata, Phys. Status Solidi C 2017, 14, 1600170.
- [26] Y. Sun, S. Lin, W. Li, S. Cheng, Y. Zhang, Y. Liu, W. Liu, Engineering 2017, 3, 452.
- [27] A. J. Ferguson, R. Farshchi, P. K. Paul, P. Dippo, J. Bailey, D. Poplavskyy, A. Khanam, F. Tuomisto, A. R. Arehart, D. Kuciauskas, J. Appl. Phys. 2020, 127, 215702.
- [28] J. Tong, Q. Jiang, A. J. Ferguson, A. F. Palmstrom, X. Wang, J. Hao, S. P. Dunfield, A. E. Louks, S. P. Harvey, C. Li, Nat. Energy 2022, 7, 642.
- [29] A. Onno, C. Reich, S. Li, A. Danielson, W. Weigand, A. Bothwell, S. Grover, J. Bailey, G. Xiong, D. Kuciauskas, W. S. Sampath, Z. C. Holman, Nat. Energy 2022, 7, 400.
- [30] D. Kuciauskas, J. M. Kephart, J. Moseley, W. K. Metzger, W. S. Sampath, P. Dippo, Appl. Phys. Lett. 2018, 112, 263901.
- [31] D. Kuciauskas, D. Albin, J. Moseley, S. Li, P. Ščajev, C. Reich, A. H. Munshi, A. Danielson, W. Sampath, C. Lee, 47th IEEE Photovoltaic Specialists Conf. (PVSC), IEEE, Piscataway, NJ 2020, pp. 0082–0084.
- [32] A. H. Munshi, C. L. Reich, A. H. Danielson, R. Pandey, D. Kuciauskas, J. Guo, S. Li, A. Shah, S. Swain, T. M. Shimpi, 47th IEEE Photovoltaic Specialists Conf. (PVSC), IEEE, Piscataway, NJ 2020, pp. 1824–1828.
- [33] M. Amarasinghe, D. Albin, D. Kuciauskas, J. Moseley, C. L. Perkins, W. K. Metzger, Appl. Phys. Lett. 2021, 118, 211102.
- [34] T. A. Fiducia, B. G. Mendis, K. Li, C. R. Grovenor, A. H. Munshi, K. Barth, W. S. Sampath, L. D. Wright, A. Abbas, J. W. Bowers, Nat. Energy 2019, 4, 504.
- [35] D. L. McGott, E. Colegrove, J. N. Duenow, C. A. Wolden, M. O. Reese, ACS Energy Lett. 2021, 6, 4203.
- [36] J. Guo, A. Sharma, A. Munshi, C. Reich, A. Danielson, W. Sampath, S. Swain, R. Klie, Microsc. Microanal. 2020, 26, 1232.
- [37] B. Good, E. Colegrove, M. O. Reese, Sol. Energy Mater. Sol. Cells 2022, 246, 111928.
- [38] Y. Zhao, M. Boccard, S. Liu, J. Becker, X.-H. Zhao, C. M. Campbell, E. Suarez, M. B. Lassise, Z. Holman, Y.-H. Zhang, Nat. Energy 2016, 1, 1
- [39] R. Pandey, A. Munshi, T. Shimpi, A. Shah, A. Bothwell, D. Kuciauskas, J. R. Sites, Sol. RRL 2021, 5, 2100126.
- [40] T. Ablekim, E. Colegrove, W. K. Metzger, ACS Appl. Energy Mater. 2018. 1, 5135.
- [41] Thin-Film Solar Cell Current Voltage and Time-Resolved Photoluminescence Simulation Model. https://www.nrel.gov/pv/solar-cell-jv-trpl-simulation-model.html, (accessed: November 2022).
- [42] A. H. Munshi, J. Kephart, A. Abbas, J. Raguse, J.-N. Beaudry, K. Barth, J. Sites, J. Walls, W. Sampath, IEEE J. Photovolt. 2017, 8, 310
- [43] D. Kuciauskas, J. N. Duenow, A. Kanevce, J. V. Li, M. R. Young, P. Dippo, D. H. Levi, 38th IEEE Photovoltaic Specialists Conf., IEEE, Piscataway, NJ 2012, pp. 001721–001726.